



Published in final edited form as:

Nanotechnology. 2010 September 10; 21(36): 365302. doi:10.1088/0957-4484/21/36/365302.

Nanofabrication of insulated scanning probes for electromechanical imaging in liquid solutions

Joo Hyon Noh¹, Maxim Nikiforov², Sergei V. Kalinin², Alexey A. Vertegel³, and Philip D. Rack^{1,2,*}

¹Department of Materials Science and Engineering, University of Tennessee, Knoxville, TN 37996-2200

²Center for Nanophase Materials Sciences, Oak Ridge National Laboratory, Oak Ridge, TN 37831

³Department of Bioengineering, Clemson University, Clemson, SC 29634-0905

Abstract

In this paper, the fabrication and electrical and electromechanical characterization of insulated scanning probes have been demonstrated in liquid solutions. The silicon cantilevers were sequentially coated with chromium and silicon dioxide, and the silicon dioxide was selectively etched at tip apex using focused electron beam induced etching (FEBIE) with XeF₂. The chromium layer acted not only as the conductive path from the tip, but also as an etch resistant layer. This insulated scanning probe fabrication process is compatible with any commercial AFM tip and can be used to easily tailor the scanning probe tip properties because FEBIE does not require lithography. The suitability of the fabricated probes is demonstrated by imaging of standard topographical calibration grid as well as piezoresponse force microscopy (PFM) and electrical measurements in ambient and liquid environments.

1. INTRODUCTION

Combining force and electrical measurements using a conductive atomic force microscopy (AFM) probe has opened a new era to simultaneously measure the topography and electrical properties, and explore the interplay between electromechanical transport, and mechanical phenomena in inorganic and biological systems on the nanometer and ultimately molecular scales [1-2]. Recent examples include: 1) the application of high resolution scanning electrochemical microscopy [3]; 2) voltage induced conformational changes of ion channels embedded in cell membranes in a buffer solution [4-5]; 3) the analysis of membrane embedded redox proteins [6]; 4) local modification of the pH [7-8]; and 5) improving the image contrast by varying the electric field or local pH [9-10].

Accessing electrochemical and electromechanical properties of biological systems requires the measurement be done in a liquid to keep the system biologically viable and mimic the real environment of cells and biomolecules. Furthermore, liquid environment allows precise control of tip-surface forces and minimization of competing capillary interactions, hence minimizing surface damage. Additionally, the measurement of electromechanical interactions in living cells in many cases needs to be performed in a multicomponent cell culture medium. However, the conductivity of the medium typically causes stray current and electromechanical reactions, which makes precise control of dc and ac probe potentials

*Corresponding author: PD Rack: prack@utk.edu.

difficult [11-12]. Because bare conductive probes with metal coatings conduct significant currents in liquid electrolytes, probes that are insulated except at the tip apex are needed in order to localize the potential and minimize the effective probe area.

The use of insulated probes for electromechanical and electrical probing in liquid environments requires (a) good dynamic properties and reflectivity of the lever, (b) good insulation except for the apex, (c) high apex conductivity, and (d) an apex geometry consistent with high resolution [11]. For these insulated probes, several approaches have been reported for scanning tunneling microscopy (STM) and AFM tips (refs. in [2,13]). Various insulator materials have been explored such as cathodic or anodic-based electrophoretic paints [14-15], poly(phenylene oxide) by electropolymerization [5], photoresist by electrophoretic deposition [16], parylene C [17], fluorocarbons [13], and silicon dioxide or silicon nitride by plasma enhanced chemical vapor deposition (PECVD) [18-19]. However, the key issue in insulated probe fabrication is how to open or expose a very small conductive area at the tip apex. In order to open the conductive area at the tip apex, focused ion beam (FIB) milling [13,17-19] or timed hydrofluoric (HF) acid wet etch [2,12,20] processes have mostly been used. In the case of FIB milling, however, it is difficult to etch the insulator selectively because of physical etching nature of FIB milling. Therefore, the underlying metal layer with high conductivity is often damaged which reduces the conductivity and the effective probe size, which is unfavorable for high resolution electrical measurements at the nanometer level. The timed HF wet etch process, while offering the advantage of batch processing, is very complex and it is difficult to etch silicon dioxide only at the tip apex. As an alternative, the combined process with focused ion beam etching (FIBE) and electron beam induced deposition (EBID) has been reported recently [11]. In that, the cantilever was coated with silicon dioxide and an opening was fabricated through the oxide at the tip apex by FIBE, and then backfilled with tungsten by EBID to create an insulated probe with a conducting tip. Although the suitability of this probe was shown through piezoresponse force microscopy (PFM) measurements in liquid, there quality of the conductive probes was limited. Specifically, the contact resistance of Si – tungsten interface is very large due to very small area of contact and low purity (~55 % of EBID tungsten).

In this study, we discuss a new approach for insulated probe fabrication using focused electron beam induced etching (FEBIE) process, which can selectively etch silicon dioxide at the nanoscale apex. Because FEBIE does not require lithography, this process can be easily implemented with any commercial AFM tip and can controllably sculpt the tip region at the nanoscale. In addition to the FEBIE process, we discuss the other relevant nanofabrication issues relative to the metallization and the insulator deposition process. Finally, the suitability of the fabricated probes is demonstrated and discussed by imaging a standard grid as well as PFM and electrical measurements in ambient and conductive liquid environments.

2. Experimental details

2.1. Tip fabrication

Commercial backside Al-coated Si atomic force microscope (AFM) cantilevers (ACD36/AIBS, MikroMasch) were used and Cr (Kurt J. Lesker, 99.9 wt.% purity, 2 in diameter, and 0.25 in thickness) was deposited using RF-magnetron sputtering. The This Cr layer acts not only as the conductive path, but also as an etch stop layer, since Cr has a high etch resistance to fluorine based etching due to low volatility of Cr-F by-products. This allowed precise tuning of deposition conditions, and is instrumental to the probe development. The deposition conditions consisted of a 25 sccm Ar flow rate, 5 mTorr pressure, and 100 W sputtering power. In order to control the density, surface roughness and thin film stress of

the Cr films, substrate bias was varied with 0, 5, and 10 W using additional RF power supply [21-22]. For Cr thickness and roughness measurements, an extra $\sim 1 \text{ cm} \times 1 \text{ cm}$ piece of silicon wafer accompanied each AFM tip deposition. Thickness and root-mean-square (rms) roughness were measured using AFM. The sheet resistance was measured using the 4-point probe method.

To insulate the scanning probes, silicon dioxide was deposited by plasma enhanced chemical vapor deposition (PECVD) (Oxford 100). The deposition parameters consisted of a flow rate of 85 sccm Ar (95%)-SiH₄ (5%) and 157 sccm N₂O, at a total process pressure of 1 Torr, 350 °C, and 20 W rf power. To make electrical contact, a portion of each the probe base was shadowed using polyimide tape during the oxide deposition. Silicon dioxide films were separately deposited on Si wafers and thicknesses were measured using an ellipsometer (JA Woollam M-2000U). Individual AFM tips were then etched in an FEI Nova 600 dual beam scanning electron microscope (SEM). Silicon dioxide at the apex tip was etched using a focused-electron-beam-induced etching (FEBIE) process [23-24]. XeF₂ vapor was locally injected using a gas injection system under electron beam irradiation. During etching, the AFM tips were tilted at 45° and periodically rotated for uniform etching. The electron beam parameters were 5 keV and 400 pA. Figure 1 schematically illustrates the insulated probe fabrication sequence.

2.2. Tip characterization

2.2.1. Tip sharpness evaluation using atomic force microscopy imaging of a standard grid—VEECO Dimension Atomic Force Microscope (AFM) equipped with a Nanoscope III controller was used for imaging in ambient. Contact mode of microscope operation with deflection set-point 0.2 – 0.5 V was used. Standard grid of sharp spikes with apex sharpness $\sim 1 \text{ nm}$ radius of curvature located 2.12 μm apart (NT-MDT, TGT1) was used.

2.2.1. Piezo-Force microscopy measurements

a. Liquid measurements: Asylum Research MFP-3D Atomic Force Microscope (AFM) with a static fluid cell was used for the imaging in MilliQ water. A piece of BiFeO₃/SrRuO₃/SrTiO₃ (50 nm/ $\sim 30 \text{ nm}$ / (100) single crystal) structure was used for PFM imaging in liquid. Single frequency lateral PFM measurements were performed by applying AC voltage using function generator (Stanford Instruments DS340) with 10 V peak-to-peak at 24 kHz; surface oscillations were measured by lock-in (Signal Recovery 7280 DSP) with sensitivity at 5 μV and time constant 5 ms. The image was acquired at a scan rate 0.15 Hz.

b. Ambient measurements: VEECO Multimode Atomic Force Microscope (AFM) equipped with a Nanonis controller was used for imaging in ambient. Single frequency lateral PFM measurements were performed by driving tip with 4 V peak-to-peak at 30 kHz (Stanford Instruments DS340); surface oscillations were measured by lock-in (Signal Recovery 7280 DSP) with sensitivity at 1 mV and time constant 5 ms. The image was acquired at a scan rate 0.25 Hz.

2.2.2. Current – distance measurements—Electrical characterization of the tip was performed using a two-terminal method. The AFM tip of interest served as one electrode, and a Au film on mica (SPI supplies 466PS-AB) served as second electrode. Au on mica was cleaned in O₂ plasma before use. The current between AFM tip and Au on mica was measured using 2 nA/V current amplifier (ORCA, Asylum Research).

3. RESULTS AND DISCUSSIONS

3.1. Tip fabrication

In order to localize the electrical potential in solution within the probed volume, the insulating layer near apex edge needs to be etched in very small area to open conductive path. Because of the ability to induce localized reactions by placement of a nanometer-sized focused electron beam [23-25], the FEBIE process was introduced to selectively etch the insulator layer at the tip apex. However, the inner Si apex can be etched spontaneously by XeF₂ vapor [26], thus an etch resistive layer with good electrical conductivity is needed between Si apex and the insulating layer. Here, Cr was chosen as an etch resistive layer because Cr has a high etch selectivity to a fluorine based etch process.

The sputtered metal thin films have intrinsic residual stress which can be varied with the deposition conditions, such as working pressure and substrate bias [21-22]. Increasing substrate bias leads the residual stress transition from tensile to compressive. The residual stress in Cr films can cause the cantilever to bend upward (tensile) or downward (compressive) depending on the residual stress, which can cause laser alignment problems during scanning probe imaging. Therefore, the effects that substrate bias and thickness have on the resultant thin film stress and cantilever bending were investigated. Figure 2 (a) – (f) show SEM images of the cantilevers as a function of substrate bias and Cr thin film thickness. Firstly, Cr films were deposited with varying substrate bias. The deposition time was 7 min and the resultant thicknesses were 18.4, 12.2 and 11.7 nm for 0, 5, and 10 W substrate bias conditions, respectively (figure 2(a)-(c)). The thickness decrease is likely due to densification and mild resputtering as the substrate bias increased. While the unbiased cantilever had a concave curvature due to the intrinsic tensile stress, the Cr film deposited with 5 W (-141 V dc self-bias) biased resulted in a cantilever with a slight convex curvature which suggests it has a modest residual compressive stress. The dashed line in the figures denotes the straight line (zero stress) condition and is included to facilitate viewing the cantilever deflection. When the substrate bias was increased up to 10 W (-166 V dc self-bias) during Cr deposition, the cantilever showed higher convex curvature which is consistent with previous reported results [21]. However, the residual stress is strongly dependent on not only substrate bias but also film thickness. In order to investigate the thickness effect on the residual stress, the deposition time was increased for the 5 W substrate bias Cr deposition. When the deposition time was increased to 10 min (16.0 nm thick), the residual compressive stress was increased, therefore the cantilever bending increased as shown in figure 2(d). When the deposition time was decreased to 5 min (9.2 nm, not shown here), no measurable cantilever bending was observed in the SEM images which suggested very small residual stress.

The precise magnitudes of the cantilever tip deflection were measured using an optical profilometer [27], and the stresses were calculated using Stoney's equation [28-29].

$$\sigma_f = \frac{F_f}{d_f w} = \frac{Y_s d_s^2}{6R(1 - \nu_s) d_f}$$

where, Y_s is Young's modulus for the substrate, d_s is the thickness of the substrate, R is the substrate curvature radius, ν_s is Poisson's ratio of the substrate, and d_f is the film thickness. Figure 2 (g) shows a typical top-view optical micrograph and profilometer scan for the AFM cantilever with 5 W substrate biased Cr thin film. Due to the fact that the profilometer scan was distorted at the end of cantilever due to the apex, the curvature radius was obtained at the middle position of cantilever using the scanning probe image processor software [30]. The thickness of back side coated Al was very thin, and hence the contribution of Al was

neglected. Figure 2 (h) shows the calculated film stress (solid symbol) and the product of stress and thickness (open symbol) as a function of thickness and substrate bias. As the thickness increased, the magnitude of the average tensile and compressive stresses both decreased. Meanwhile, the product of stress and thickness was increased, which is inversely proportional to the radius of curvature and commonly used to interpret substrate curvature measurements [31]. Figure 2 (e) and (f) shows the cantilever SEM images after silicon dioxide deposition for the 0 and 5 W substrate bias, respectively. The PECVD silicon dioxide was deposited for 2 min with a thickness of ~ 138 nm, which shows a mild compressive residual stress. Therefore, the cantilever with the Cr film deposited with zero substrate bias and a tensile residual stress was compensated with the SiO₂ film and is no longer bent. In the case of 5 W bias the original compressive stress is enhanced and thus the oxide coated Cr cantilever has a higher convex curvature. For a PECVD process, the residual stress, which consists of an intrinsic and thermal stress, is strongly related to the deposition parameters and substrate temperature [32]. While the detailed mechanisms is subject for future studies, here we were able to minimize the effect of the compressive stress introduced by the silicon dioxide by decreasing the silicon dioxide deposition time (and thickness) to 1 min (69 nm).

In addition to the thin film stress, the roughness of the deposited Cr thin film is also an important factor for AFM tip fabrication. A smoother surface is more favorable for high resolution. The surface roughness was measured by AFM for the scan size of 500×500 nm as a function of substrate bias (not shown). While the unbiased Cr film has a root-mean-square (rms) roughness of 0.583 nm, the 5 W and 10 W biased Cr films have rms roughnesses of 0.283 nm and 0.308, respectively. Compared to unbiased Cr film, smoother surface and thinner thickness indicates the densification in biased Cr film due to energetic particle bombardment. The densification using substrate bias has another merit. Because the Cr film is used as the etch resistive layer, it has to block XeF₂ penetration to prevent spontaneous etching of the Si apex. If there are voids in the thin film, XeF₂ can etch the Si apex through the voids. For instance, we tested the etch resistance of commercial Pt or Au coated Si tips but all tips failed due to the spontaneous etching of the Si apex, as shown in figure 3. The etching is likely due to defects, such as voids, in the Pt and Au. Figure 3 (a) and (b) show the etched tip images taken from the top and 45° tilted view, respectively, for the commercial Pt coated tip with 150 nm-thick SiO₂ film deposited by PECVD. This tip was tilted with 45° degree during etching. The void like defects in Pt film are clearly shown in figure 3 (b). Figure 3 (c) and (d) show another failed tip images taken from top and 45° tilted view, respectively, for the commercial Pt coated tip with 30 nm-thick SiO₂ film deposited by sputtering. This tip was etched with top-down configuration. One plane of the apex was aggressively spontaneously etched by the XeF₂.

Clearly a critical thickness is required in order to prevent XeF₂ penetration, however, the radius of curvature of the tip is increased with increasing thickness. Because substrate bias can suppress void formation through densification, and thus require a thinner etch resistant film, very thin biased Cr film is favorable to maintain a sharp Si apex required for high resolution imaging. However, further increase of substrate bias caused an increase in the roughness. The roughness of the 10 W biased Cr film increased to 0.308 nm compared to 0.283 nm of 5 W biased film, which is likely due to higher re-sputtering.

Additionally, the resistivity was investigated for the unbiased and biased films because the conductivity of Cr film is also important. The resistivity was calculated from the sheet resistance using 4 point probe method. Figure 4 shows the resistivity as a function of substrate bias. While the unbiased Cr film had a resistivity of 3.5×10^{-4} Ω-cm, the 5 W and 10 W biased Cr films have resistivity of 2.8 and 3.1×10^{-5} Ω-cm, respectively. The resistivity of biased Cr films is comparable to the bulk Cr resistivity of 1.29×10^{-5} Ω-cm

[33]. As mentioned above, the low resistivity of biased films is likely due to densification through energetic particle bombardment and sputtering of adsorbed oxygen (or other contaminants). As demonstrated for the metal layer, there are important trade-offs that have to be evaluated such as stress, surface roughness, conductivity, and etch resistance.

In our experiments, Cr films with 5 W substrate bias were chosen for an optimized etch resistive layer with low resistivity and roughness. After the PECVD silicon dioxide was deposited on Cr films, the AFM tips were processed using the FEBIE process. Silicon dioxide can be only etched by XeF_2 with assistance by ion or electron irradiation [26]. The silicon dioxide focused electron beam etching mechanism with a XeF_2 precursor is suggested to proceed via a two-step etch process [24]. This model involves the reduction process by the electron-stimulated desorption of oxygen at the silicon dioxide surface, and subsequent silicon etching by XeF_2 . Therefore etching only can occur in the electron-beam irradiation region. The etch rate is strongly dependent on the electron beam energy, current, XeF_2 pressure, and pixel dwell time. In our experiment, the etching was performed in the area scan mode with 50 ns pixel dwell time. Figure 5 shows SEM images at each process step. For figure 5, the Cr and SiO_2 deposition times were 7 and 2 min, respectively, which corresponded to 12.2 nm and 138 nm, respectively. From the SEM images, as shown in figure 5 (a) – (c), the tip radii of curvature were measured to be approximately 18, 30, and 285 nm for bare, Cr, and SiO_2 deposited tip, respectively. Before etching, the tip position was adjusted to the XeF_2 gas injector as close as possible ($<500 \mu\text{m}$) and the magnification was set as $\times 400,000$. Figure 5 (d) – (f) show SEM images during different stages of the FEBIE process. In order to realize uniform etching, the tip was tilted 45° and periodically rotated. The final images of the etched tip are shown in figure 5 (g) – (i), taken from the top, 45° tilt, and 90° rotation view, respectively. The revealed apex has dimensions of 284 nm height and 164 nm width. There was not any evidence for inner Si attack by XeF_2 from the high magnification SEM images. The estimated SiO_2 thickness at apex was approximately 255 nm from the figure 5 (h), although the SiO_2 thickness was 138 nm measured at flat sample deposited separately. This enhanced thickness is likely due to field enhancement at the apex during the PECVD process.

These observations indicate that there is a trade-off in performance and fabrication with increased insulator thickness. For thicker films, lower leakage currents and higher breakdown voltages are realized. However, longer processing times, more compressive stress, and possible interference of the insulator sidewalls with the scanning probe measurement are detriments of thicker insulators. Figure 6 shows the SEM images at each process step for a tip with a reduced silicon dioxide deposition thickness (1 min of SiO_2 deposition time) which corresponded to 69 nm thickness measured on the flat substrate and estimated to be 123 nm at the apex tip (figure 6 (f)). In order to reduce the tip radius, the Cr deposition time was also decreased to 5 min, which corresponded to 10.5 nm. The tip radii of curvature were measured to be ~ 22 and 140 nm after Cr and SiO_2 deposition, respectively. The final images of the uniformly etched tip are shown in figure 6 (c) and (g), taken from the top and 45° tilt view, respectively. The exposed apex has dimensions of 199 nm height and 166 nm width.

3.2. Tip characterization: imaging, piezo-force microscopy (PFM) and electrical characterization of the isolated tip

In order to evaluate the quality of the tip prepared according to the procedure described above the tip was used for imaging of standard grid as well as for PFM and electrical measurements (see Experimental description for the detailed description of techniques). Figure 7 (a) shows the tapping mode AFM image of the standard grid consisting of sharp spikes with radius of curvature ~ 1 nm regularly spaced on the surface, which allows estimation of the tip radius because the broadening of the spike on the image happens due to

the finite tip radius [11]. The inset of figure 7 (a) shows the three-dimensional representation of tip shape. The tip radius determined from this measurement is ~ 30 nm (figure 7 (b)). The radius determined from SEM images was 22 nm (figure 6 (c) and (f)).

Isolated probes are intended for probing of electrical and electromechanical characteristics of samples with high spatial resolution. To achieve this goal, two related conditions must be satisfied. First, the probes should deliver a potential from the sample to the probed area, in our case it is the tip apex. Second, the current flowing between tip and surface should be measurable. The delivery of voltage to the tip apex was tested by measuring mechanical response of $\text{BaFeO}_3/\text{SrRuO}_3/\text{SrTiO}_3(100)$ (BFO/SRO/STO) structure to electrical excitation (so-called inverse PFM response). Current voltage characteristics were measured for a bare probe and insulated probe in ambient and liquid (MilliQ H_2O).

The measurements of lateral piezo-force response from $\text{BaFeO}_3/\text{SrRuO}_3/\text{SrTiO}_3(100)$ (BFO/SRO/STO) structure was used as a first step of electrical characterization of the tip. Previous studies show that such a sample has a rich in-plane domain structure [34]. Figure 8 shows the PFM measurements performed in air revealed rich domain structure. Such observation proves that voltage applied to the sample reaches very end of the tip. The tip radius can be estimated independently from these measurements by measuring the width of the domain wall. The width of domain wall in PFM experiments on BFO/SRO/STO structure is usually ~ 5 nm, thus, any broadening of the domain wall observed with PFM beyond 5 nm is a result of domain wall broadening due to the finite tip radius. Line profile from the phase image is presented on figure 8. To quantify the resolution, the domain-wall profile has been fit to the function $R^- + (R^+ - R^-) \cdot \tanh[(x-x_0)/(w/2)]$, where R^+ (R^-) is the response on the left (right) of the domain wall centered at x_0 and w is the width of the domain wall [35]. The width of the domain wall was calculated to be ~ 32 nm, the apparent width of the domain wall corresponds well to the radius of the probe used for wall probing, as shown in figure 7 (b).

As discussed earlier, the targeted application of isolated tips are electromechanical measurements in liquid, thus, lateral PFM imaging of BFO/SRO/STO was done in H_2O to demonstrate the applicability of these probes for such measurements (figure 8). The domain pattern is visible indicating that the probing voltage reaches the end of the tip in liquid. A decrease of the probing volume of BFO due to the formation of electrical double layer in water (Debye layer ~ 10 nm thick in H_2O pH ~ 7) is responsible for the decrease of PFM response (more detailed discussion of this effect can be found in ref. [36]).

Several types of electrical characterization measurements were done on the insulated probe. First, the contact resistance between insulated/Au-coated probes and Au was measured in ambient. The contact resistance for the insulated probe was ~ 62 k Ω , comparable to the conventional Au-coated probes. The difference in resistance between insulated and Au-coated probe was quite small indicating applicability of this probe for electrical measurements. In liquid we compared measurements of current between insulated/Au-coated probes and Au counter electrode as a function of tip – surface distance. We found that parasitic current between from Au-coated probe is ~ 2 nA at 30 mV, when the tip is located far away from the surface. Parasitic current decreases more than 10 times (to ~ 3 nA at 500 mV) when the insulated probe was used. For insulated probes we measured the dependence of the current on tip – surface distance (figure 9 and 10). As the tip approaches the surface (3 μm and closer) the electrical current between tip and surface starts to increase indicating the leakage of the current through the liquid barrier (figure 9). The contact resistance decreases with an increase in voltage between electrodes (figure 10 (b)).

To conclude, isolated probes can be used for PFM imaging and electrical characterization of the materials in ambient as well as in liquid.

4. CONCLUSION

In summary, we have demonstrated the fabrication of insulated probes for electrical and electromechanical imaging in liquids using FEBIE process which can selectively silicon dioxide at the nanoscale apex. In addition to FEBIE, we discuss the other relevant nanofabrication issues relative to the metallization and the insulator deposition process. Finally, the suitability of the fabricated probes is demonstrated and discussed by imaging of standard grid as well as PFM and electrical measurements. This fabrication process of insulated probes can be easily implemented with any commercial AFM tip because FEBIE does not require lithography process.

Acknowledgments

This work was supported in part by NIH grant No. RR024449. A portion of this research was conducted at the Center for Nanophase Materials Sciences, which is sponsored at Oak Ridge National Laboratory by the Division of Scientific User Facilities, U.S. Department of Energy.

Reference list

1. Macpherson JV, Unwin PR. Combined Scanning Electrochemical–Atomic Force Microscopy. *Anal Chem* 2000;72:276–85. [PubMed: 10658320]
2. Frederix P, Gullo MR, Akiyama T, Tonin A, de Rooij NF, Staufer U, Engel A. Assessment of insulated conductive cantilevers for biology and electrochemistry. *Nanotechnology* 2005;16:997–1005.
3. Zoski CG, Liu B, Bard AJ. Scanning electrochemical microscopy: Theory and characterization of electrodes of finite conical geometry. *Anal Chem* 2004;76:3646–54. [PubMed: 15228336]
4. Drake B, Prater CB, Weisenhorn AL, Gould SAC, Albrecht TR, Quate CF, Cannell DS, Hansma HG, Hansma PK. Imaging crystals, polymers, and processes in water with the atomic microscope. *Science* 1989;243:1586–9. [PubMed: 2928794]
5. Engel A, Muller DJ. Observing single biomolecules at work with the atomic force microscope. *Nat. Struct. Biol* 2000;7:715–8. [PubMed: 10966636]
6. Frederix PLTM, Bosshart PD, Akiyama T, Chami M, Gullo MR, Blackstock JJ, Dooleweerd K, de Rooij NF, Staufer U, Engel A. Conductive supports for combined AFM-SECM on biological membranes. *Nanotechnology* 2008;19:384004.
7. Bullard JW, Kershner RJ, Cima MJ. Scanning probe characterization of localized pH changes on a sapphire surface in the presence of an applied field. *Mater. Res. Soc. Symp. Proc* 2004;782:A3.1.1–6.
8. Jang JW, Sanedrin RG, MasPOCH D, Hwang S, Fujigaya T, Jeon YM, Vega RA, Chen XD, Mirkin CA. Electrically biased nanolithography with KOH-coated AFM tips. *Nano Lett* 2008;8:1451–5. [PubMed: 18376868]
9. Muller DJ, Engel A. The height of biomolecules measured with the atomic force microscope depends on electrostatic interactions. *Biophys. J* 1997;73:1633–44. [PubMed: 9284330]
10. Muller DJ, Fotiadis D, Scheuring S, Muller SA, Engel A. Electrostatically balanced subnanometer imaging of biological specimens by atomic force microscope. *Biophys. J* 1999;76:1101–11. [PubMed: 9916042]
11. Rodriguez BJ, Jesse S, Seal K, Baddorf AP, Kalinin SV, Rack PD. Fabrication, dynamics, and electrical properties of insulated scanning probe microscopy probes for electrical and electromechanical imaging in liquids. *Appl Phys Lett* 2007;91:093130.
12. Akiyama T, Gullo MR, de Rooij NF, Tonin A, Hidber HR, Frederix P, Engel A, Staufer U. Development of insulated conductive probes with platinum silicide tips for atomic force microscopy in cell biology. *Japan. J. Appl. Phys* 2004;43:3865–7.
13. Wiedemair J, Balu B, Moon JS, Hess DW, Mizaikoff B, Kranz C. Plasma-deposited fluorocarbon films: Insulation material for microelectrodes and combined atomic force microscopy-scanning electrochemical microscopy probes. *Anal Chem* 2008;80:5260–5. [PubMed: 18510344]

14. Durig U, Gimzewski JK, Pohl DW. Experimental-Observation of Forces Acting during Scanning Tunneling Microscopy. *Phys. Rev. Lett* 1986;57:2403–6. [PubMed: 10033716]
15. Frederix PT, Hoogenboom BW, Fotiadis D, Muller DJ, Engel A. Atomic force microscopy of biological samples. *Mrs Bull* 2004;29:449–55.
16. Lantz MA, O'Shea SJ, Welland ME. Characterization of tips for conducting atomic force microscopy in ultrahigh vacuum. *Rev. Sci. Instrum* 1998;69:1757–64.
17. Kueng A, Kranz C, Mizaikoff B, Lugstein A, Bertagnolli E. Combined scanning electrochemical atomic force microscopy for tapping mode imaging. *Appl Phys Lett* 2003;82:1592–4.
18. Kranz C, Friedbacher G, Mizaikoff B, Lugstein A, Smoliner J, Bertagnolli E. Integrating an Ultramicroelectrode in an AFM Cantilever: □ Combined Technology for Enhanced Information. *Anal Chem* 2001;73:2491–500. [PubMed: 11403290]
19. Lugstein A, Bertagnolli E, Kranz C, Kueng A, Mizaikoff B. Integrating micro- and nanoelectrodes into atomic force microscopy cantilevers using focused ion beam techniques. *Appl Phys Lett* 2002;81:349–51.
20. Gullo MR, Frederix PLTM, Akiyama T, Engel A, deRooij NF, Stauffer U. Characterization of microfabricated probes for combined atomic force and high-resolution scanning electrochemical microscopy. *Anal Chem* 2006;78:5436–42. [PubMed: 16878880]
21. Misra A, Nastasi M. Limits of residual stress in Cr films sputter deposited on biased substrates. *Appl Phys Lett* 1999;75:3123–5.
22. Thornton JA, Hoffman DW. Stress-Related Effects in Thin-Films. *Thin Solid Films* 1989;171:5–31.
23. Randolph SJ, Fowlkes JD, Rack PD. Focused, nanoscale electron-beam-induced deposition and etching. *Crit Rev Solid State* 2006;31:55–89.
24. Randolph SJ, Fowlkes JD, Rack PD. Focused electron-beam-induced etching of silicon dioxide. *J Appl Phys* 2005;98:034902.
25. Lassiter MG, Rack PD. Nanoscale electron beam induced etching: a continuum model that correlates the etch profile to the experimental parameters. *Nanotechnology* 2008;19:455306.
26. Winters HF, Coburn JW. Etching of silicon with XeF₂ vapor. *Appl Phys Lett* 1979;34:70–3.
27. Guo Q, Li M, Li Y, Shi L, Chong TC, Kalb JA, Thompson CV. Crystallization-induced stress in thin phase change films of different thicknesses. *Appl Phys Lett* 2008;93:221907–3.
28. Ohring, M. *Materials science of thin films*. Academic Press; Boston: 1992.
29. Stoney GG. The Tension of Metallic Films Deposited by Electrolysis. *Proc. R. Soc. London, Ser. A* 1909;82:172–5.
30. Scanning Probe Image Processor (SPIP). Ver. 5.1.1. <http://www.imagemet.com/>
31. Seel SC, Thompson CV, Hearne SJ, Floro JA. Tensile stress evolution during deposition of Volmer-Weber thin films. *J Appl Phys* 2000;88:7079–88.
32. Tarraf A, Daleiden J, Irmer S, Prasai D, Hillmer H. Stress investigation of PECVD dielectric layers for advanced optical MEMS. *J. Micromech. Microeng* 2004;14:317–23.
33. Kulkarni AK, Chang LC. Electrical and structural characteristics of chromium thin films deposited on glass and alumina substrates. *Thin Solid Films* 1997;301:17–22.
34. Balke N, Choudhury S, Jesse S, Huijben M, Chu YH, Baddorf AP, Chen LQ, Ramesh R, Kalinin SV. Deterministic control of ferroelastic switching in multiferroic materials. *Nat. Nanotechnol* 2009;4:868–75. [PubMed: 19893529]
35. Bode M. Spin-polarized scanning tunnelling microscopy. *Rep. Prog. Phys* 2003;66:523–82.
36. Rodriguez BJ, Jesse S, Baddorf AP, Kalinin SV. High resolution electromechanical imaging of ferroelectric materials in a liquid environment by piezoresponse force microscopy. *Phys. Rev. Lett* 2006;96:4.

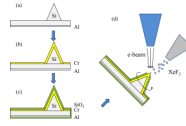


Figure 1.
Schematic illustration of the insulated probe fabrication sequence.

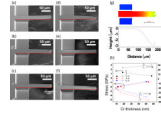


Figure 2.

(a) – (d) SEM images of the cantilevers as a function of substrate bias and Cr thin film thickness; (a) 0 W substrate bias, 18.4 nm, (b) 5 W substrate bias, 12.2 nm, (c) 10 W substrate bias, 11.7 nm, (d) 5 W substrate bias, 16.0 nm, and (e) – (f) SEM images of the cantilevers after 138 nm-thick PECVD SiO₂ deposition with Cr film of (e) 0 W substrate bias, 18.4 nm and (f) 5 W substrate bias, 12.2 nm. (g) Typical top-view optical micrograph and profilometer scan for the cantilever with 5 W substrate biased Cr thin film, (h) Cr film stress (solid symbol), and product of stress-thickness (open symbol) as a function of Cr thickness at 0, 5, and 10 W substrate bias.

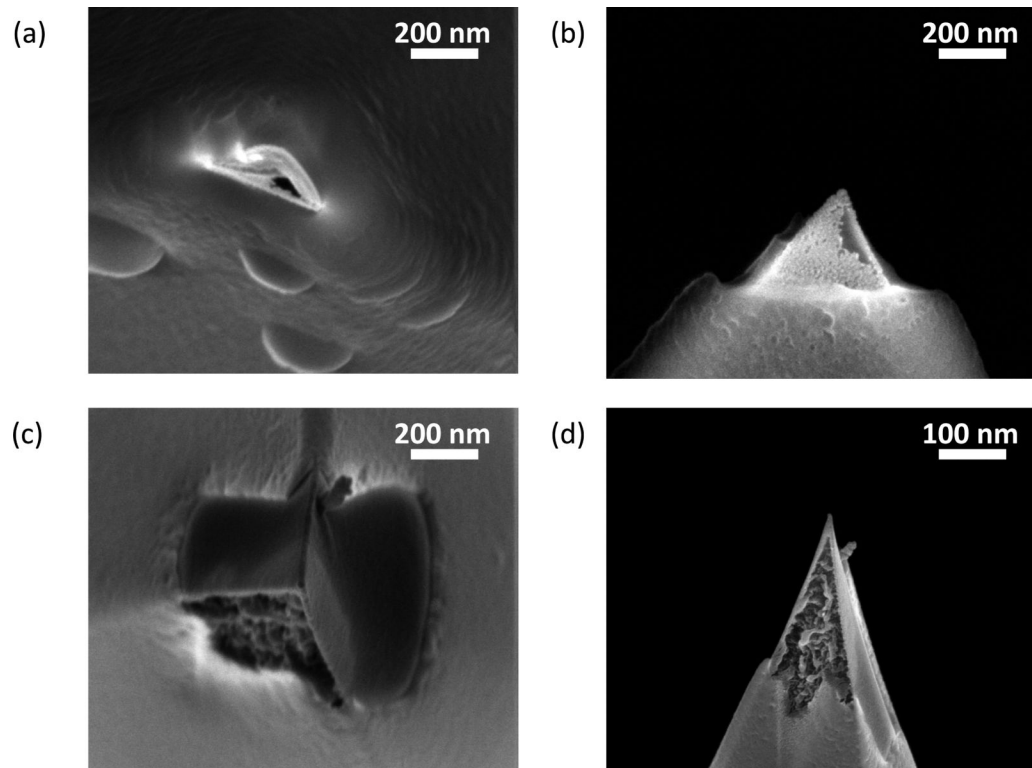


Figure 3. Etched tip SEM images for the commercial Pt coated tip with 150 nm-thick SiO₂ film deposited by PECVD taken from the (a) top and (b) 45° tilted view, and for the commercial Pt coated tip with 30 nm-thick SiO₂ film deposited by sputtering taken from the (c) top and (d) 45° tilted view.

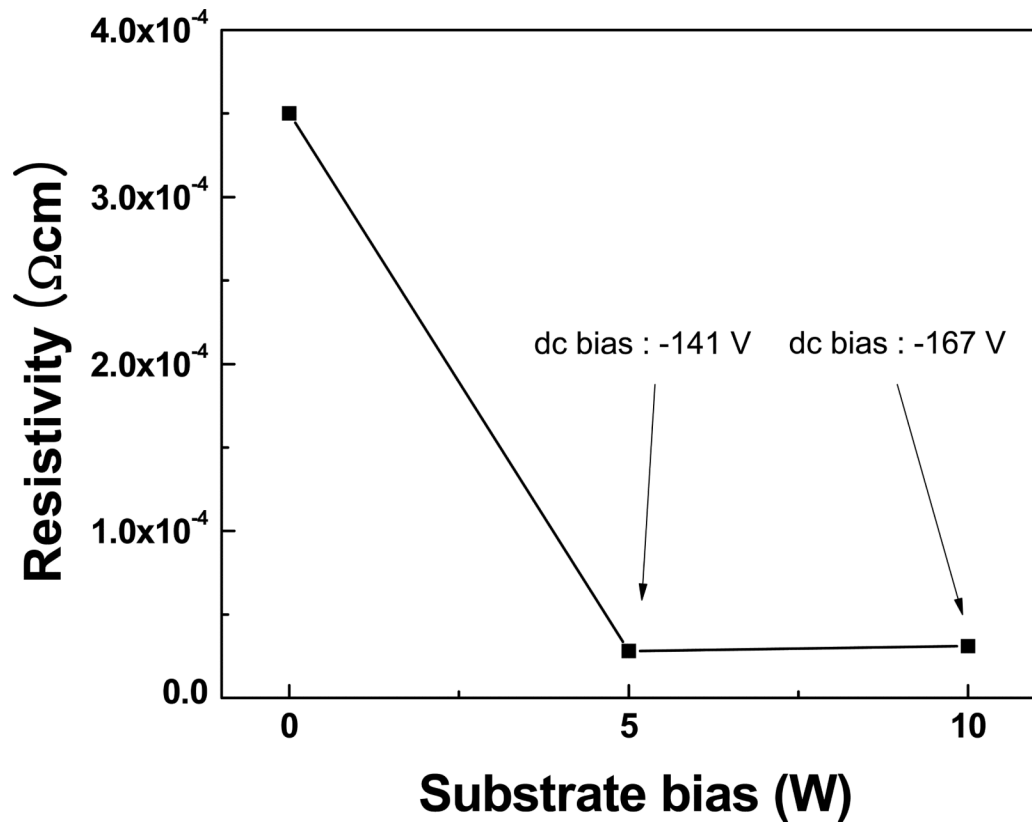


Figure 4.
Cr resistivity as a function of substrate bias.

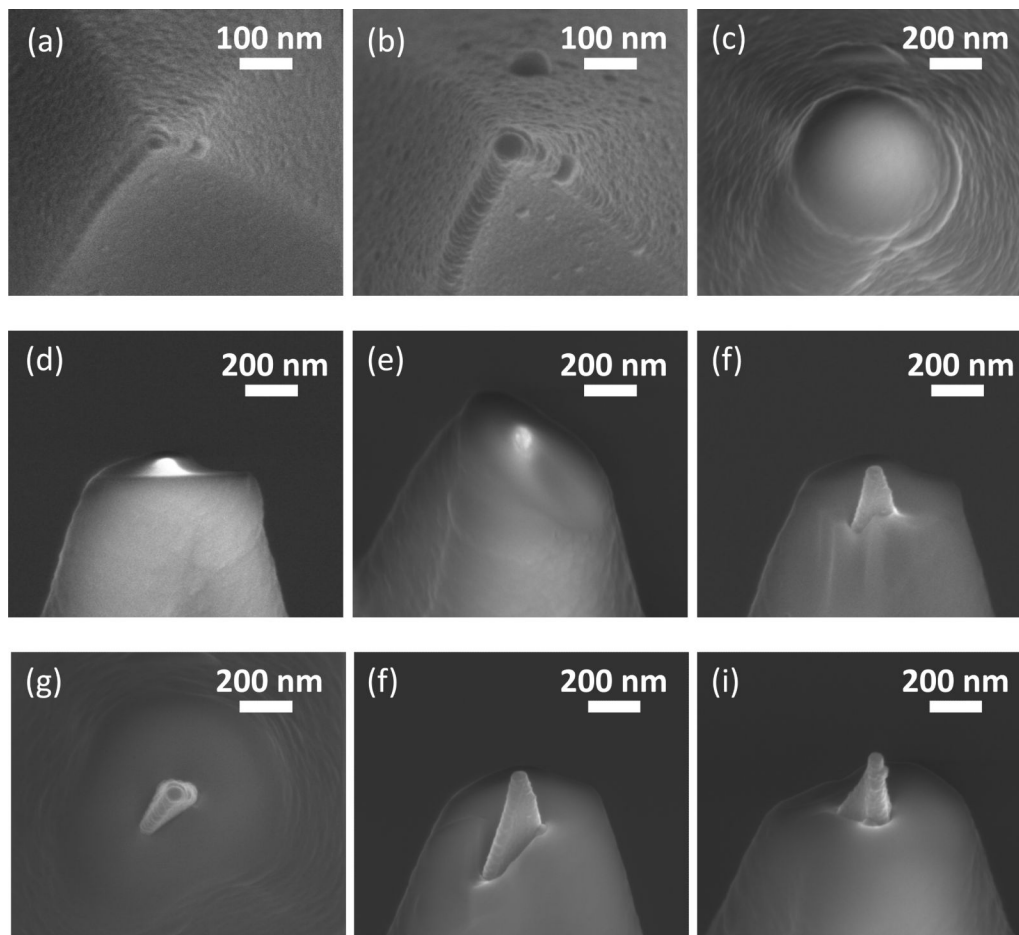


Figure 5.

(a) – (c) SEM images at each deposition step; (a) bare, (b) 5 W biased Cr, and (c) SiO₂ deposited tip. The Cr and SiO₂ deposition times were 7 and 2 min, which corresponded to 12.2 nm and 255 nm, respectively. (d) – (f) SEM images during different stages of the FEBIE process. (g) – (i) SEM images for the final etched tip; (g) top, (h) 45° tilt, and (i) 90° rotation view.

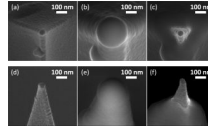


Figure 6. SEM images at each process step; [(a) and (d)] 5 W biased Cr, [(b) and (e)] SiO₂ deposition, and [(c) and (f)] after etching. The Cr and SiO₂ deposition times were 5 and 1 min, which corresponded to 10.5 nm and 123 nm, respectively; (a) – (c) top, and (d) –(f) 45° tilt view.

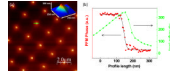


Figure 7.

(a) Tapping mode AFM image of the standard grid of sharp spikes (Inset: three-dimensional representation of tip shape). (b) Topography line profile (green line in figure 9 (a)) and PFM phase line profile (red line in figure 10). Tip radius obtained from topography profile (~ 30 nm) corresponds well with tip radius (32 nm) obtained from PFM phase fitting.

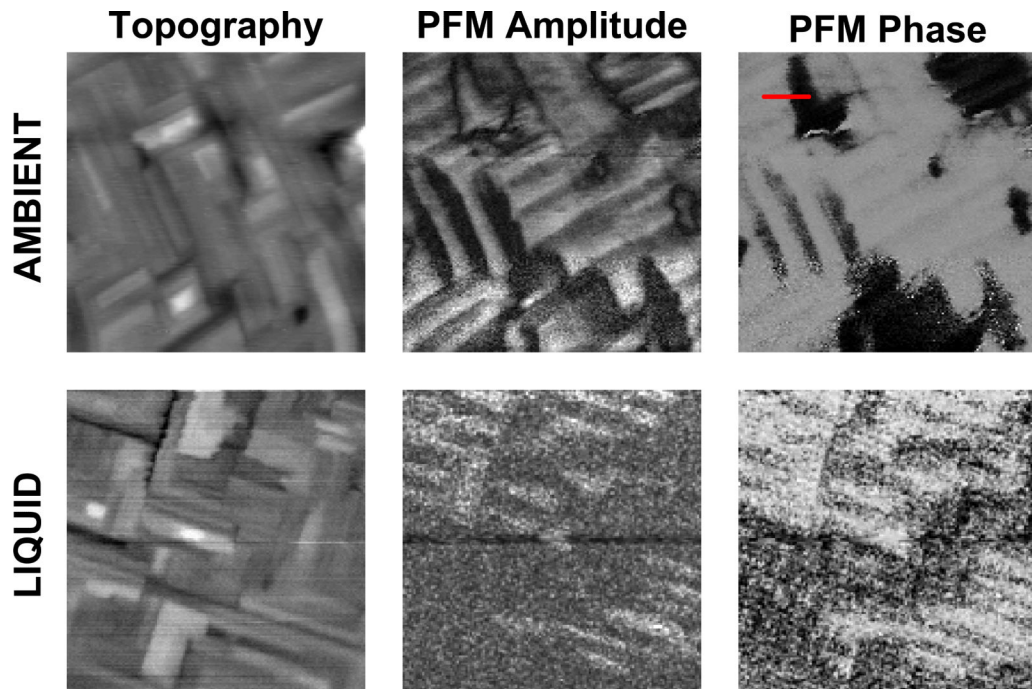


Figure 8. Lateral Piezo-Force Microscopy on BFO/SRO/STO (100) structure. Ambient and liquid measurements show rich domain pattern characteristic for thick (50 nm) BFO films. Tip radius is estimated ~ 32 nm.

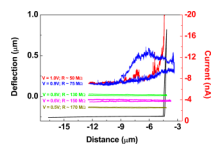


Figure 9. Current – distance curves in liquid taken at different voltages. Current was measured using two electrode method. AFM tip served as one electrode and Au film served as second electrode.

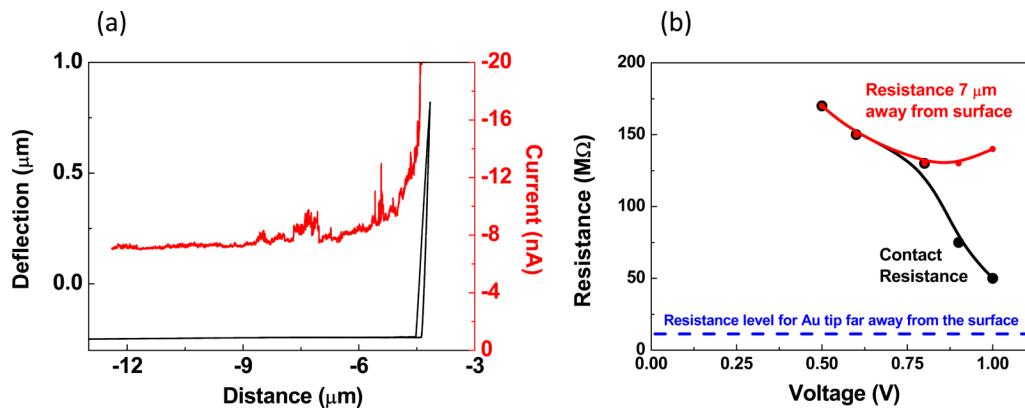


Figure 10.

(a) Current – distance curve in liquid taken at 1 V. A Significant increase in current is realized when the tip is in mechanical contact with the surface and proves the formation of good electrical contact. (b) Comparison of the system resistance for the tip far away from the surface and in contact with the surface. Resistance for bare Au tip is given as reference.